

www.acsnano.org

Mie Resonance Engineering in Meta-Shell Supraparticles for Nanoscale Nonlinear Optics

Joong Hwan Bahng, Saman Jahani, Douglas G. Montjoy, Timothy Yao, Nicholas Kotov, and Alireza Marandi*



Cite This: ACS Nano 2020, 14, 17203-17212



ACCESS

III Metrics & More



Supporting Information

ABSTRACT: Supraparticles are coordinated assemblies of discrete nanoscale building blocks into complex and hierarchical colloidal superstructures. Holistic optical responses in such assemblies are not observed in an individual building block or in their bulk counterparts. Furthermore, subwavelength dimensions of the unit building blocks enable engraving optical metamaterials within the supraparticle, which thus far has been beyond the current pool of colloidal engineering. This can lead to effective optical features in a colloidal platform with ability to tune the electromagnetic responses of these particles. Here, we introduce and demonstrate the nanophotonics of meta-shell supraparticle (MSP), an all dielectric colloidal superstructure having an optical nonlinear metamaterial shell conformed onto



a spherical core. We show that the metamaterial shell facilitates engineering the Mie resonances in the MSP that enable significant enhancement of the second harmonic generation (SHG). We show several orders of magnitude enhancement of second-harmonic generation in an MSP compared to its building blocks. Furthermore, we show an absolute conversion efficiency as high as 10⁻⁷ far from the damage threshold, setting a benchmark for SHG with low-index colloids. The MSP provides pragmatic solutions for instantaneous wavelength conversions with colloidal platforms that are suitable for chemical and biological applications. Their engineerability and scalability promise a fertile ground for nonlinear nanophotonics in the colloidal platforms with structural and material diversity.

KEYWORDS: colloids, nanostructures, metamaterials, nonlinear optics, Mie resonances

olloidal nanoparticles (CNPs) and their assemblies exhibit a cohort of electromagnetic (EM) resonances and couplings, facilitating them as essential optical actuating platforms in bio/-chemical sensing, imaging, and photocatalytic reactions. 1-6 Their processing versatility enable easy integration into photonic and solid-state devices^{7,8} as modular light sources. When assembling the colloidal nanoparticles into colloidal superstructures, holistic optical responses are observed that are not found in an individual building block or in their bulk counterparts. Notwithstanding, CNPs that enable instantaneous and efficient nonlinear harmonic conversion of electromagnetic (EM) stimuli could provide solutions to the remaining important challenges in their photoactivation and -actuation. For example, wavelength requirements to trigger a photostimulation could bring limitations due to insufficient light penetration into the reaction media and biological tissues. 10,11 Delivering optical energy through the ambient media within its specific transparency windows that could trigger the target photoresponses via instantaneous wavelength conversions could

immensely broaden the scope of the operations while enhancing its procedural compatibilities and efficiencies. 12–15

Recently, several advanced strategies have been employed to enhance optical wavelength conversions in nanostructures. A large subset of such strategies are focused on high index materials that are architected via top-down nanofabrication. ^{16–34} On the other hand, synthetic challenges exist in realizing dexterous colloidal platforms with high index materials and their bottom-up fabrication. As such, communities have explored low index nanocolloids for optical nonlinear conversions. ^{35–39} However, limitations in their structural

Received: August 24, 2020 Accepted: November 24, 2020 Published: December 8, 2020





diversities and complexities constrains their engineerability for nonlinear nanophotonics.

Here, we demonstrate a pragmatic approach to enhance optical nonlinear conversions with low index $\chi^{(2)}$ CNPs by assembling them into a colloidal superstructure in the form of a synthetic metamaterial shell conformed onto a dielectric core sphere, which can be denoted as the meta-shell supraparticles (MSP), Figure 1a. In comparison to individual $\chi^{(2)}$ CNPs, their

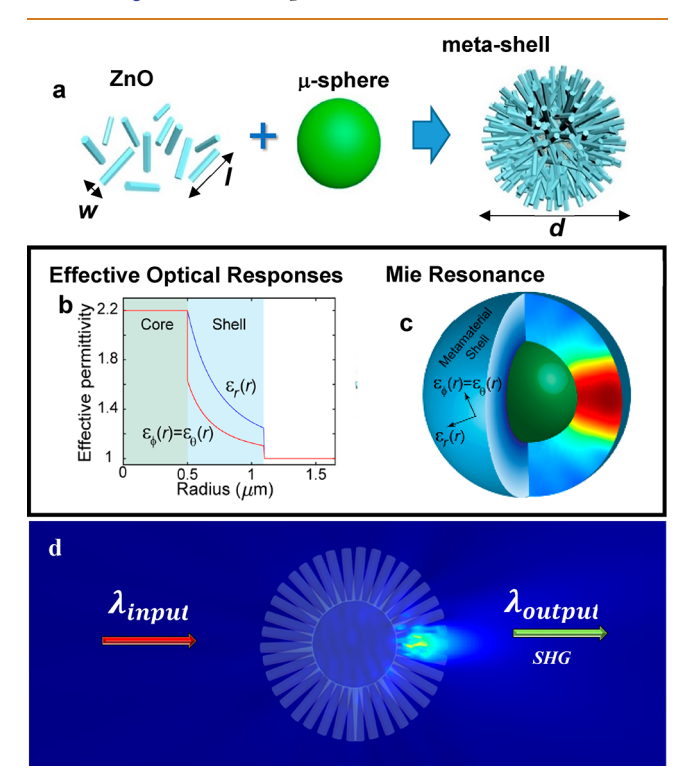


Figure 1. Nonlinear nanophotonics with colloidal meta-shell supraparticle (MSP). (a) The MSP, of diameter d, is synthesized by assembling ZnO nanorods (NRs), of width w and length l, into a spherical array, forming a shell of metamaterials (meta-shell), conformed onto a dielectric μ -sphere; (b) the meta-shell features radial graded index and spherical anisotropy profile that provides additional degrees of freedom (c) with which to engineer Mie resonances within the MSP, (d) through which mode profiles, both spectral and spatial, are designed to significantly enhance the SHG conversion efficiencies of the ZnO NRs and also to control its radiation pattern.

assembly into an MSP increases the density of Mie resonances and their combinations for $\chi^{(2)}$ nonlinear optical interactions. The anisotropy and the graded-index profile of the metamaterial shell (Figure 1b) in these particles can be utilized for engineering the collective behavior of these Mie resonances, allowing for a significant enhancement in the second order nonlinear optical wavelength conversions (Figure 1b-d).

RESULTS AND DISCUSSIONS

The MSP is realized through one-pot chemical synthesis (Supporting Information (SI) 1.1). We have previously demonstrated hierarchical colloidal superstructures with high quality and yield, using multiple materials selections with various constitutive properties, shapes, and dimensions. ^{40–42} Such a synthetic versatility enabled us to engineer structures via simple procedural adjustments. The MSP can have varieties

of core spheres with tailored meta-shell nanotopography comprised of vertically oriented ZnO nano rods (NRs) as the noncentrosymmetric $\chi^{(2)}$ material⁴³ (a few examples in Figure 2d,e (SI 1.1)).

First, we carried out linear light scattering measurements by the MSPs in aqueous dispersion and realized that their extinction lineshapes do not correlate with either the ZnO NRs or the core μ -spheres, Figure 2f. The spectra feature a broadband peak (P₁) in the visible wavelengths and a narrower peak (P₂) in the ultraviolet range. When P₂ is approximately at the second harmonic of the P₁, the overlap of the EM modes at both the fundamental and the second-harmonic wavelengths suggests opportunities for wavelength conversion. This emergent spectral behavior arising from multitude of Mie resonances can be fine-tuned by adjusting the meta-shell corrugation geometry or its core dimensions, ⁴⁴ Figure 2g-i. These experimental findings on the linear response of the MSPs are verified with finite difference time domain (FDTD) full-wave simulations. We created a model MSP (SI 2.2) that mirrors the experimental construct based on a polystyrene (PS) core sphere with an overall diameter of $d = 2.2 \mu m$ (Figure 2a), that is, MSP2.2. The model replicates the imperfect orthogonal orientation of the ZnO NRs. Numerical results of extinction cross-section $\sigma_{\rm ext}$ of MSP2.2 are in agreement with the experimental measurements, as depicted in Figure 2j,k (SI 2.2-2.4). Note that, due to solution based chemical synthesis nature of the MSP, there will be particle to particle variations which accounts for the slight mismatch in the scattering peaks between the experiment and the simulation. For studying the nonlinear nanophotonics of the MSP, the PS cores were subsequently replaced with SiO₂ core owing to its superior mechanical and thermal stability against high power laser.

The linear response of the meta-shell supraparticle, which consists of a metamaterial shell on a core, is enriched by the density of its Mie resonances. While ED, EO, and MD modes are supported in the core-only silica sphere ($d_{\text{core}} = 1 \, \mu \text{m}$) at λ = 1550 nm, our theoretical analysis suggests that the meta-shell particle accommodates a different set of Mie resonances including electric-dipole (ED), -quadrupole (EQ), -octupole (EO), -hexadecapole (EH), and magnetic-dipole (MD), -quadrupole (MQ), -octupole (MO) modes (SI 4.2), as shown in Figure 3. These Mie resonances and their interferences can be tuned in the MSP to lead to a hot spot with strong electric field strength |El. Such a behavior is similar to formation of a photonic nanojet in simple low-index geometries; 45-51 however, a significant portion of this hot spot forms in the shell and its |E| strength can be much larger than that of the core alone (see an example with 2-fold |E| enhancement, SI 3.2).

Engineering the Mie resonances of the MSP and their interferences can be achieved through tuning the radial graded-index profile as well as the angular anisotropy of the metamaterial shell (Figure 4). The key distinction of the metamaterial shell compared to the conventional metamaterials is its spherical construct of high aspect-ratio unit building blocks. Such arrangement leads to a radial graded-index profile. Our analytical calculations (SI 4.1) show that changing the graded-index profile enables us to change the scattering behaviors of the particle at both the fundamental and the second harmonic wavelengths, Figure 4a–c. Moreover, the effective index of the shell near the periphery of the particle (due to lower ZnO NR density) generates an excellent

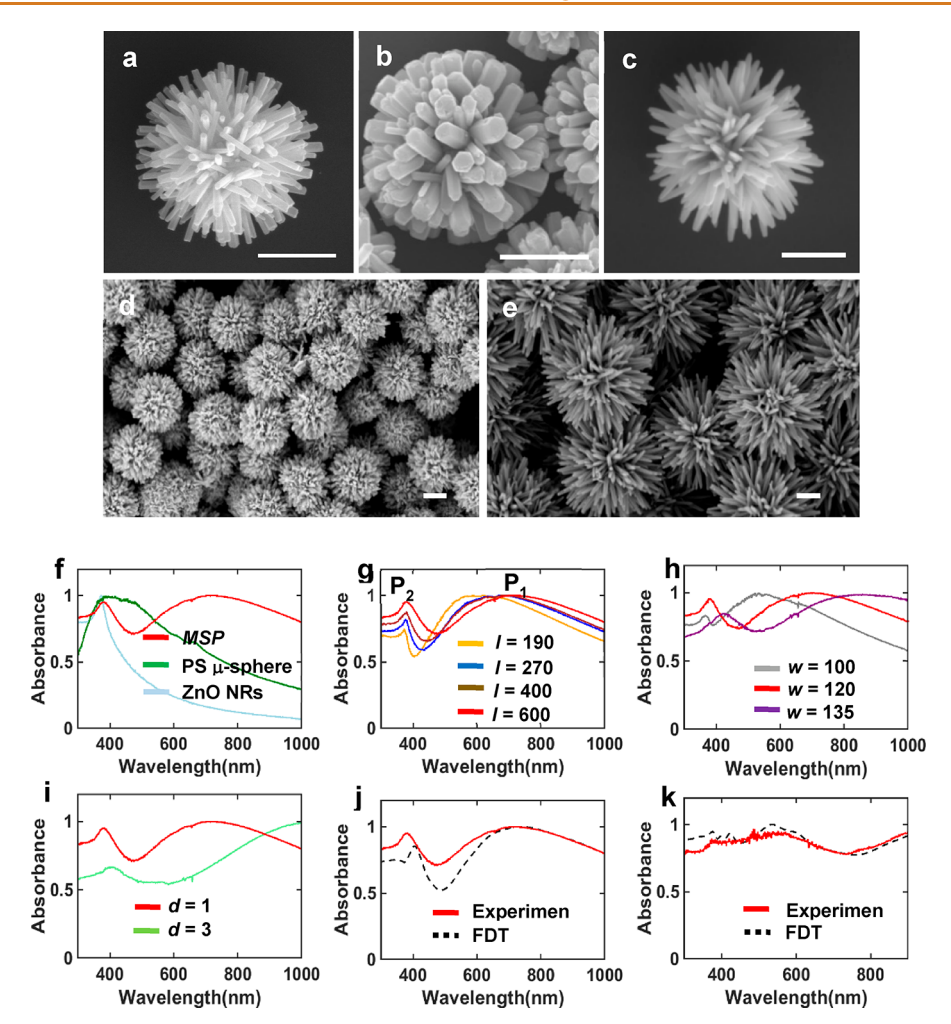


Figure 2. Structural engineering of MSP. a-c, scanning electron microscopy (SEM) images of the MSP synthesized with a polystyrene (PS) μ -sphere core (diameter, $d=1~\mu$ m) having diverse geometries and dimensions of its unit building block ZnO NRs that constitute the metashell; d,e, MSP synthesized with a SiO₂ μ -sphere template ($d=1~\mu$ m) and having ZnO NR (d) length $l\approx 600$ nm, designated MSP2.2 and (e) $l\approx 1290$ nm, designated MSP3.58; f-i, spectral tuning is achieved by adjusting the corrugation geometry in the meta-shell, (f) peak normalized (P.N.) extinction spectra (A.U.), in aqueous dispersion, of ZnO NRs, $d=1~\mu$ m PS μ -sphere and MSP; P.N. extinction spectra of MSP with (g) varying spike lengths, $l\approx 190$ nm, $l\approx 270$ nm, $l\approx 400$ nm, $l\approx 600$ nm and (h) varying spike widths, $w\approx 100$ nm, $w\approx 120$ nm, $w\approx 135$ nm, and (i) varying core diameters, $d=1~\mu$ m, $d=3~\mu$ m; j-k, Overlap in the spectral line shape between the extinction cross-section ($\sigma_{\rm ext}$) of a model MSP from the FDTD full wave simulation, and the extinction spectra from the experimental measurement, for both suspended in (j) water and in (k) air. Since absorption for ZnO is minuscule above $\lambda=360$ nm (as is the case for both polystyrene and silica), the spectrum shown here is essentially the scattering spectrum arising from different resonances of the nanostructure. All scale bar: 1 μ m.

impedance-matched interface which can help to reduce the backscattering of the incident light at the interface, leading to improvement in the light delivery to the shadow side of the supraparticle. As the graded-index tapers to free space, maximal spectral overlap in the ED and the MD mode is achieved across a broad spectrum, Figure 4c (SI 4.3). This can facilitate spatial overlap of the photonic nanojet at both the fundamental and the second-harmonic wavelengths, Figure 4d. Improvement in the spatial and spectral overlaps can lead to enhancement of the second-harmonic generation in the photonic nanojet, and its efficient forward propagation, as shown in Figure 4e,f. Hence, the radial graded index profile in the MSP can be instrumental in enhancing the SHG and its directionality that is suitable for applications in chemical and biological settings.

The spherical arrangement of orthogonal ZnO NR array in the metamaterial shell also leads to radial anisotropy in the spherical coordinate, which does not appear in natural dielectrics. Such an anisotropy is expected to provide additional degrees of freedom in the overall optical responses. S2-60 In the metamaterial shell, the spherical anisotropy enables fine-tuning the spatial location of the photonic nanojet hotspot. This capability can be utilized for enhancing the nonlinear conversion efficiency by overlapping the hot spot with the highest densities of $\chi^{(2)}$ nanostructures. Increasing the anisotropy (decreasing the ε_{θ_i} while keeping $\varepsilon_{\rm r}$ constant) can move the hotspot toward the core interface, Figure 4g-i, hence contributing to the enhancement of the nonlinear conversion process.

The SHG efficiency (η) can be decomposed to the SHG efficiency of contributing modes $(\eta_{\text{SHG},n})$ as 61

$$\eta = \sum_{n} \eta_{\mathrm{SHG},n} = \sum_{n} \left| \frac{E_{2\omega,n}}{E_{\omega}^{2}} \right|^{2} = \sum_{n} \left| \frac{4\widetilde{\eta}_{n}^{2}}{\delta \omega_{n}^{2} + (\omega_{n}/2Q_{n})^{2}} \right|^{2}$$

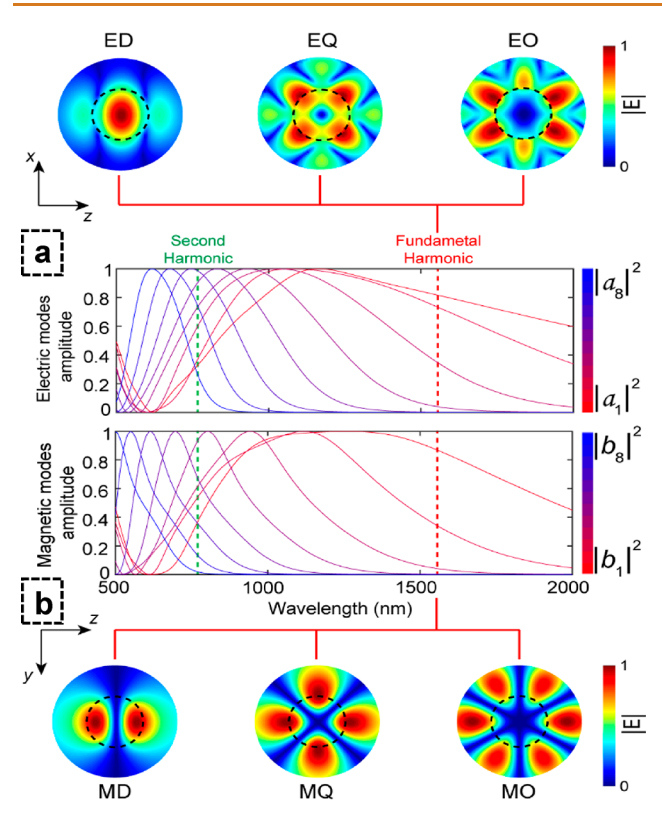


Figure 3. Mie resonance enrichment with meta-shell. Scattering coefficients of (a) electric and (b) magnetic multipoles in the MSP calculated from analytical modeling and Mie theory; compared to a core μ -sphere, the density of Mie resonances is enriched in the presence of a circumambient meta-shell. See SI 4.2 for scattering coefficients corresponding core sphere. Here, a_n and b_n are the scattering coefficients of electric and magnetic dipole in the nth order, respectively.

where $E_{2\omega,n'}$ is the field envelope of nth mode at the second harmonic (2ω) resonating at ω_n $(\delta\omega_n=2\omega-\omega_n)$ with a quality factor of Q_n . E_ω is the envelope of the excitation field at the fundamental harmonic, and $\tilde{\eta}_n$ is the nonlinear coupling between the input at fundamental harmonic and the second-harmonic output defined as the field overlap between the nth mode at the second-harmonic and the input excitation in the nonlinear region. The strength of the overlap between each Mie mode and the hot-spot at the fundamental harmonic, the quality factor, and the detuning of the center of the resonance of each modes from the second-harmonic define the contribution of each mode on the output signal.

Our analysis based on the Mie theory considering the graded index profile and the spherical anisotropy of the meta-shell (SI 4.1, 4.2) matches the full-wave FDTD simulations and explains the superior nonlinear performance of the meta-shell supraparticles (SI 3.2). Without the meta-shell, the SiO₂ core sphere generates a photonic nanojet whose region of peak |E| is confined within the core sphere, Figure 4j. In the presence of a meta-shell featuring a graded index profile only, the peak |E| at the hotspot region is enhanced by an approximate 2-fold, but localized at the outer peripheries, Figure 4k. While the peak |E| is higher without the spherical anisotropy in the meta-shell, ascribing spherical anisotropy to the meta-shell fine-tunes the spatial location of the hotspot volume toward, but exterior to, the core interface, at which the density of the $\chi^{(2)}$ nanostructures are at its highest, Figure 4l. Overall, the

simulations show an approximate 4-fold increase in the peak |E| at the hotspot in the MSP compared to that of the incident light |E| (SI 3.3, Figure S8).

For the experimental measurement, we utilized two-photon laser scanning confocal microscope with input wavelength centered around $\lambda=900$ nm. As the commercial scanning microscope was not appropriate for quantifying the SHG conversion efficiency, we utilized custom-built NLO microscopy employing femtosecond laser with input wavelength at $\lambda=1550$ nm. Hence, we present our calculation results both at $\lambda=1550$ nm (Figure 3) and $\lambda=900$ nm (Figure 4) while designating the corresponding alternative to the Supplementary Information. Importantly, we note that the nature of the enhancement in the conversion efficiency remains the same for both wavelengths.

We initially characterized the SHG from the MSP using pulsed input sources in a commercial laser scanning microscope. At identical input powers and detection settings, we are unable to measure the SHG from independently synthesized colloidal ZnO NRs (SI 6.2). This indicates an enhancement in the SHG from the MSP compared to the ZnO NR building blocks.

While the SHG from individual ZnO NRs were below our minimum detectable signal, we used full-wave FDTD simulations to estimate the enhancement in the normalized SHG conversion efficiencies η (W⁻¹) of different configurations of ZnO NRs, Figure 5c–f. In carrying out the simulation, we simplified the optical nonlinearity of ZnO NR to have effective second order susceptibility ($\chi^{(2)} = 15 \text{ pm/V}$), whose value was within the ranges of previously reported values⁶² (SI 5.2). When placing a single $\chi^{(2)}$ ZnO NR at the shadow side of a SiO₂ core μ -sphere, the photonic nanojet enhances its η by an approximate 7-fold, Figure 5d. In the presence of the meta-shell featuring the graded index and spherical anisotropy profile but without the $\chi^{(2)}$, there is an additional 66-fold increase in η , Figure 5e. Finally, when $\chi^{(2)}$ is assigned to the meta-shell in its entirety, there is an additional 87-fold increase in η , Figure 5f. Hence, there is an approximate 10^4 -fold enhancement in the SHG η between an MSP2.2 and a single ZnO NR (SI 6.3). It is also worth noting that the spherical symmetry of the meta-shell particle makes it insensitive to polarization variations of a linearly polarized input.63

Next, we quantified the experimental value of the η (W⁻¹) by the MSP2.2 utilizing custom-built NLO microscopy, Figure 5b (SI 7.1–7.6). Taking into account the SHG signal collected in the reflection mode, η averages to 9.97 × 10⁻¹² W⁻¹. The full-wave FDTD simulations replicating the experimental setup (SI 7.5) resulted in η = 8.53 × 10⁻¹² W⁻¹ which closely approximates the experimental measurements.

Taking into account the SHG signal collected in the forward-scattered mode, the maximum η reached 8.05×10^{-11} W⁻¹. This corresponds to 1.08×10^{-7} of absolute conversion efficiency, which is the highest achieved by solution processed dielectric colloidal particles reported thus far, displaying 5 orders of magnitude improvement compared to that reported from the BaTiO₃ nanoparticles, ³⁵ and also displays 2 orders of magnitude improvement compared that observed with a colloidal hybrid plasmonic superstructure. ⁶⁴ It should be noted that the maximum absolute conversion efficiency was achieved with the maximum available power at the particles, which was far from the damage threshold and any saturation in the efficiency, Figure 5b. While the average input power of

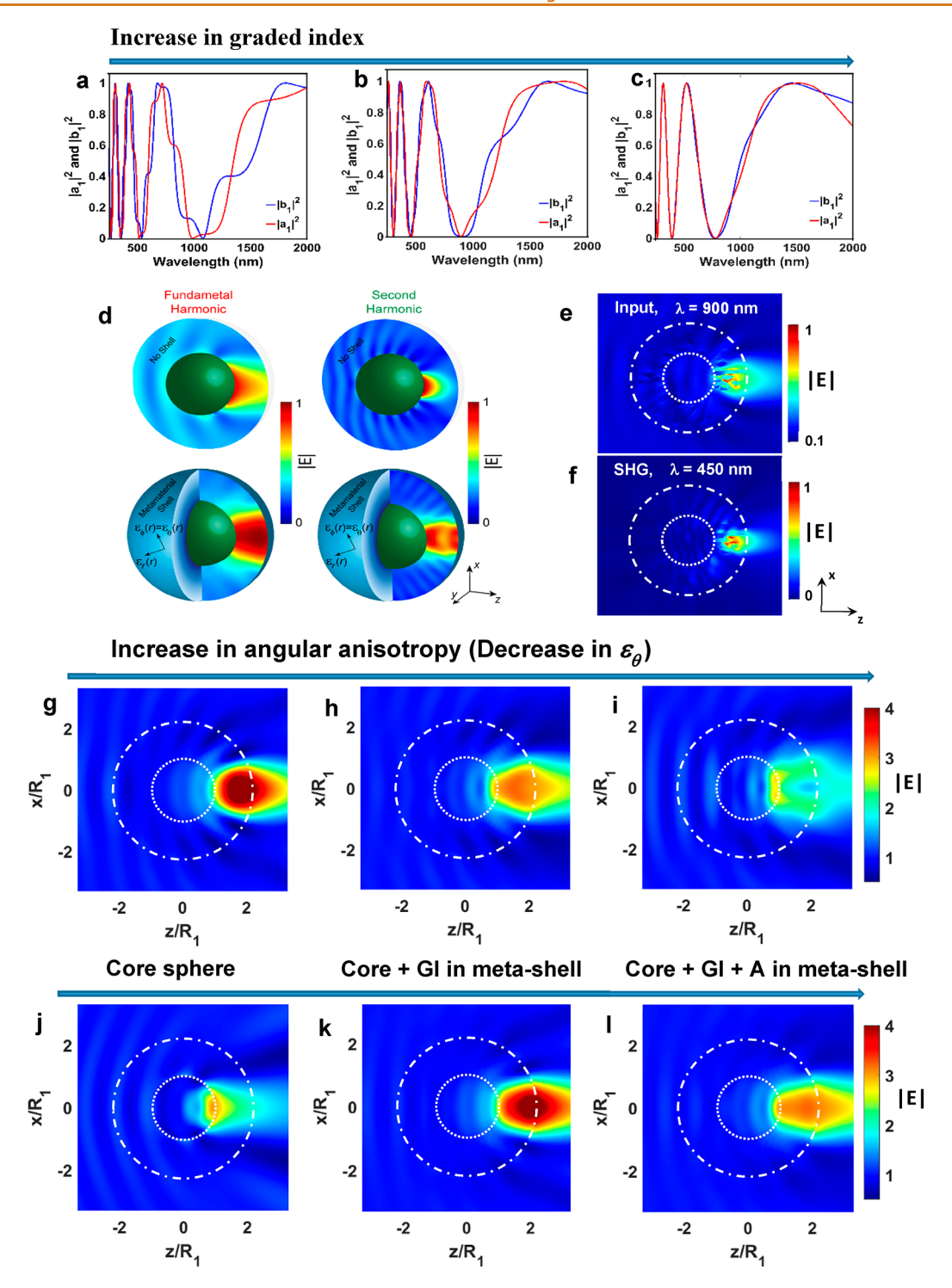


Figure 4. Mie resonance engineering with meta-shell. The diameter of the core sphere is $d_{\text{core}} = 1 \,\mu\text{m}$, thickness of the meta-shell is $t_{\text{shell}} = 600$ nm. The permittivity of the sphere is $\varepsilon_{\text{core}} = 2.2$; a - c, increase in the index gradient increases the broadband spectral overlap between the electric dipole (ED) and the magnetic dipole (MD) mode that spans several higher order harmonics, (a) $\varepsilon_{r, \text{ shell}}$: 2.2, (b) $\varepsilon_{r, \text{ shell}}$: 2.2 \rightarrow 1; a_1 and b_1 are the scattering coefficients of electric and magnetic dipole in the first order, respectively. (d) Multimode interferences leading to the formation of photonic nanojet hotspot and their spatial overlap at both fundamental and the second harmonic wavelengths; e-f, FDTD full wave simulation, at $\lambda = 900$ nm, showing (e) photonic nanojet formed by the model MSP2.2 upon light incidence and (f) enhanced forward scattering in the SHG radiation pattern by the model MSP, alike to a photonic nanojet. The details of the nonlinear optics simulations with the FDTD can be found in the 5–7; g-i, Increase in the angular anisotropy shifts the hotspot toward the core sphere interface, (g) $\varepsilon_{\theta, \text{ shell}}$: 2.2, (h) $\varepsilon_{\theta, \text{ shell}}$: 1.5, (i) $\varepsilon_{\theta, \text{ shell}}$: 1; Here, the radial anisotropy is kept constant, $\varepsilon_{r, \text{ shell}} = 2.2$; j-l, photonic nanojet features, calculated from the analytical modeling, for (j) the core sphere, (k) core sphere with meta-shell having gradient index (GI) feature and (l) core sphere with meta-shell having both the gradient index and anisotropy (A) features. See SI 4.3, Figure S10 for identical plots with input $\lambda = 1550$ nm.

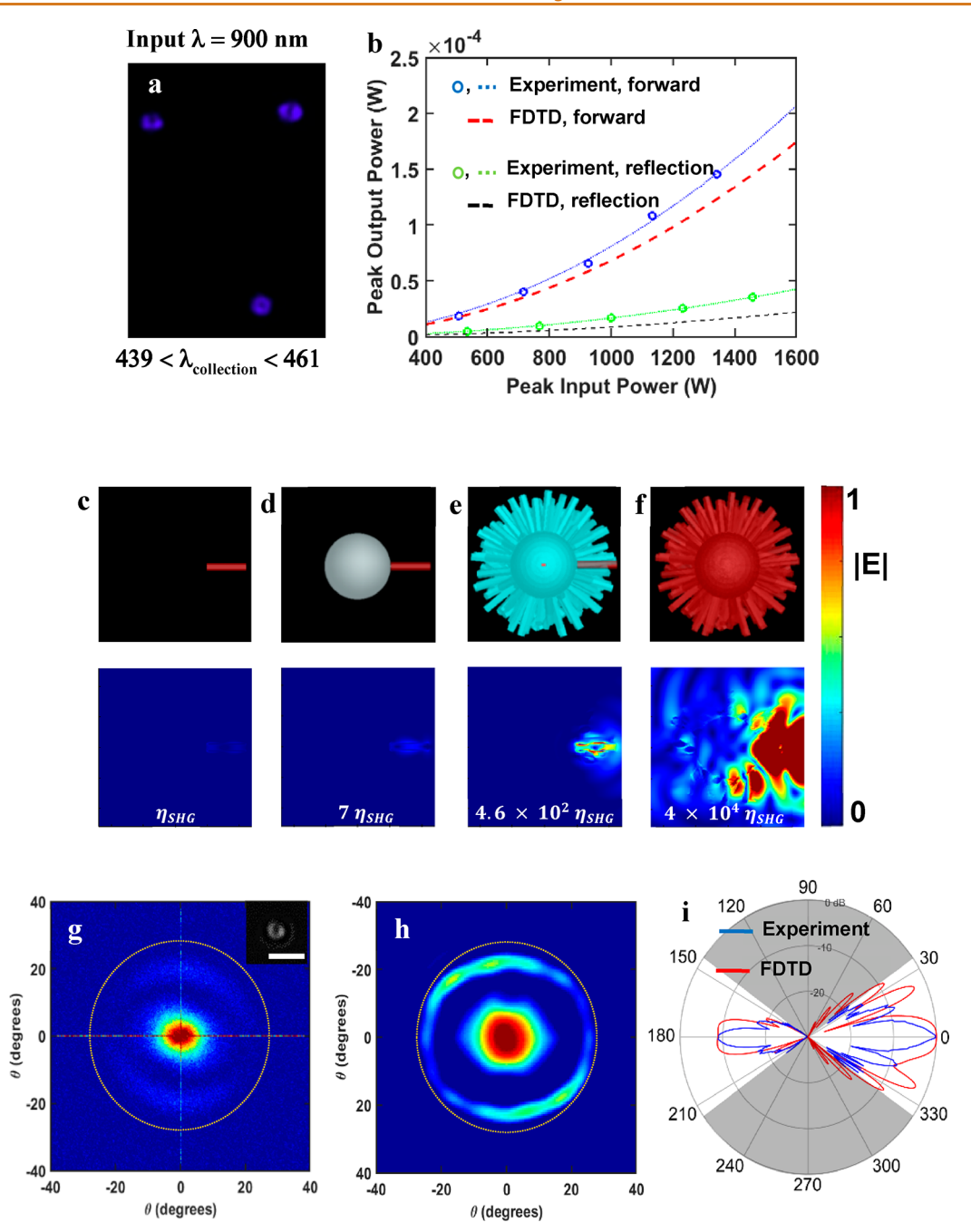


Figure 5. Second harmonic generation of light by the MSP. (a) confocal microscopy image of the SHG by the MSP2.2 (see SI 6.1 details); (b) Experimental values of forward scattered and reflected SHG output power, measured from custom built optical nonlinear microscope (SI 7.1–7.3), display quadratic dependence to the input power. For SHG signal collected in the reflection mode, η ranged between 6.17 × 10⁻¹² W⁻¹ and 1.53 × 10⁻¹¹ W⁻¹ (N = 29). For the SHG signal collected in the forward scattered mode, η ranged between 4.87 × 10⁻¹¹ W⁻¹ and 8.05 × 10⁻¹¹ W⁻¹ (N = 5). Sample having the highest SHG conversion values collected in the reflection mode and in the forward scattered mode are plotted in the graph as demonstration. The dotted green line (R = 0.9997) and the dotted blue line (R = 0.996) are fit to the quadratic curves ($y = \eta x^2$) for reflected and forward scattered SHG, respectively. The FDTD simulation of the predicted quadratic relationships for the reflected ($\eta = 8.53 \times 10^{-12}$ W⁻¹) and forward scattered ($\eta = 6.81 \times 10^{-11}$ W⁻¹) SHG are also plotted; c–f, FDTD simulation, for input pulse centered at $\lambda = 1550$ nm, showing 4 orders of magnitude enhancement in the SHG conversion efficiencies η between a model MSP2.2 and a ZnO NR; Farfield radiation pattern of the forward scattered SHG from (g) the experiment (the inset is the experimental SHG image) and from the (h) FDTD simulation. Dotted circle represents the angle of collection for the forward scattered SHG; (i) The directivity plot showing enhanced forward scatter of the SHG. The MSP employed for the study here are samples from Figure 2d (MSP2.2); All scale bar: 5 μ m.

femtosecond pulses at the particles, $P_{\rm in,avg'}$ for the above measurement was 46 mW, we measured that the MSP2.2 could withstand $P_{\rm in,avg}$ up to 1 W at $\lambda=1550$ nm. It is worth noting that we have observed laser-induced damage in some defective

particles leading to clear changes in the optical images of the particle. The SHG measurement from both the reflected and the forward-scattered detection scheme exhibit quadratic dependence to the input power, Figure 5b.

The η measurement from the forward-scattered mode averages to $\eta = 6.43 \times 10^{-11} \text{ W}^{-1} \text{ (N = 5), indicating a}$ forward to backward scattering ratio (F/B) of 6.45 with the current measurement setup. The high F/B accords with the findings from the FDTD simulations. Farfield directivity polar plot, Figure 5i, derived by taking the FFT of the secondharmonic images, Figure 5g, shows enhanced forward scattering of SHG (see SI 7.6 for farfield pattern of reflected SHG). The FDTD full-wave simulation of MSP2.2 with identical experimental parameters yields $\eta = 6.81 \times 10^{-11} \text{ W}^{-1}$ for the forward-scattered SHG and the F/B = 7.98. Furthermore, taking into account the total SHG in all directions, the MSP2.2 in the simulation exhibits $\eta = 1.48 \times$ 10⁻¹⁰ W⁻¹. Consistency among our 3D full-wave simulations, analytical studies, and experimental results illustrates the efficacy of our developed techniques for future studies in the colloidal nonlinear nanophotonics.

CONCLUSION

The presented meta-shell approach for enhancing enhancing optical nonlinear processes in nanostructures is in sharp contrast with the ongoing nonlinear nanophotonic efforts. While most of the efforts utilize high Q-factor Mie resonances confined within the structures usually comprised of high-index materials, our meta-shell approach utilizes collective interferences of high-density low-Q-factor modes in low-index materials, which lead to formation of strong hotspots that is utilized to enhance the conversion efficiency of the $\chi^{(2)}$ elements in the MSP. Furthermore, the metamaterial shell allows for engineering the Mie resonances of the suprapaticle to maximize the spatial overlap of the hotspot with the regions having highest density of the $\chi^{(2)}$ colloidal elements. The presented platform utilizes the low-index wide-bandgap colloidal supraparticles made of ZnO for nonlinear optical wavelength conversion. While ZnO does not have a large $\chi^{(2)}$ compared to other commonly used nonlinear materials, its well-developed chemical synthesis in the colloidal platforms makes it compatible with a wide array of scientific and industrial processes. Furthermore, the demonstrated concept can be extended to metallic structures to utilize plasmonic resonances to further expand the possibilities of nonlinear nanophotonics with colloidal platforms. 65 Combining chemical and optical properties that arise from the MSP packaged into a single supraparticle could further expand development of the colloidal nonlinear nanophotonics to chemistry and biology.

METHODS

Chemical Synthesis of MSP. The colloidal meta-shell supraparticles (MSP) are constructed via aqueous colloidal synthesis under mild synthetic conditions. Initially, positively charged ZnO nanoparticles (NPs) (Sigma-Aldrich) are electrostatically adsorbed onto negatively charged colloidal core spheres. The core spheres utilized for the construction of the MSP are polystyrene (PS) and silica (SiO₂) μ -spheres. We utilized carboxyl functionalized PS μ -spheres (Polysciences Inc.) that is imparted with interfacial negative charges. In order to impart interfacial negative charges to the SiO₂ μ -spheres, we overlaid the particle with polyelectrolyte poly(allylamine hydrochloride)-poly(acrylic acid) coating sequence in a layer-by-layer approach. The interfacial coating of ZnO NPs function as seeds from which ZnO nanorods (NR) are grown in vertical orientations via a combination of hydrothermal and sonochemical processes. Synthetic methods to impart interfacial negative charges to the SiO₂ μ-spheres will be described in detail in the forthcoming publication "Photocatalytic Hedgehog Particles for High Ionic Strength Environments: Electric Field Catalysis without Electrodes". 66 In a typical synthesis that constructs the meta-shell of the MSP2.2 (1 μm in core diameter, 600 nm in meta-shell thickness, total MSP diameter of 2.2 μm), the ZnO NP coated core spheres are immersed in ZnO precursors, comprised of 25 mM of zinc nitrate hexahydrate (Zn(NO_3)_2.6H_2O, Sigma-Aldrich) and 25 mM hexamethylenetetramine (C_6H_12N_4, Sigma-Aldrich), dissolved in aqueous solution. ZnO NRs are grown by subjecting the mixture to hydrothermal (90°) and sonochemical energy for 90 min. The length, thickness and the densities of the ZnO NRs in the meta-shell are easily tailored by adjusting their growth conditions, such as the growth time, ZnO precursor concentrations and the seeding density. The SiO_2 μ -spheres are synthesized by the well-known Stober process. The synthesized MSP are maintained as a dispersion in aqueous environment.

FDTD Simulations. Full wave simulations are carried out using Lumerical FDTD to characterize optical extinction properties of the MSP, near-field distributions at different wavelengths and nonlinear conversion efficiencies. First, we created a model MSP composed of either a SiO₂ or a PS core of diameter $d = 1 \mu m$ and the meta-shell consisting a spherical array of ZnO NRs (length l = 600 nm, thickness w = 120 nm) that mirrors the experimental construct. Computer aided design software was used to reconstruct a model MSP with imperfect orthogonalization of ZnO NRs to mirror the experimental construct and to remove artifacts due to symmetry that is not present in the experimental construct (see SI 2.2 and 2.4). Total-field scattered-field (TFSF) source was utilized to obtain extinction cross section of the MSPs and to estimate the second harmonic conversion efficiencies of the MSP. The simulation setup is configured to emulate the experimental conditions such as the objective NA and the pulsed input sources (see SI 6 and 7). We simplified the optical nonlinearities of ZnO NR to have isotropic susceptibility tensor having an effective $\chi^{(2)} = 15 \text{ pm/V}$. Ref 41 reports a range of nonlinear coefficients from $d_{\text{eff}} = 2 \text{ pm/V}$ to 15 pm/V. We have chosen a median value ($d_{\text{eff}} =$ 7.5 pm/V) from the reported range to numerically approximate second harmonic conversion of the MSP.

Confocal Microscopy. The SHG measurement was also carried out with confocal microscopy (Zeiss LSM 880 with two photon laser) in which the MSP are irradiated with femtosecond pulses (140 fs, 80 MHz) centered at $\lambda=900$ nm and at 5% of its maximum available power. In order to fully immerse the MSP within the spotsize, a low NA (0.16) 5× objective was use. The SHG intensities obtained from the images are subtracted by the background noise, normalized by the gain settings, followed by normalization with the square of the input power reading.

NLO Microscopy. The schematic in SI Figure S20 (7.1) depicts the nonlinear optical (NLO) microscopy setup constructed to detect the SHG generated by the MSP. SI Table S1 (7.1) shows the optical components employed in the setup. Ultrashort pulse frequency comb (Menlo Systems, τ = 80 fs, $f_{\rm rep}$ = 250 MHz) centered at $\lambda_{\rm in}$ = 1550 nm is used as the input source. The input pulse is subject to a continuously variable neutral density filter wheel to obtain variable input average power. The input beam is guided into a 50× objective (Mitutoyo Plan APO NIR, NA = 0.42) and focused onto a single particle on the sample slide with a spot size $d_f \approx 2.6 \mu m$. A collimated LED white light source was incorporated to locate and focus the input pulse into individual MSP. The backscattered SHG is subject to a pair of filters to remove the input light and the third harmonic generation. A 1" VIS lens was used to focus the SHG onto a photodiode power sensor. The total average power of the backscattered SHG is then determined by accounting for the power loss through each optical component. The transmission values of each optical component that the SHG passes through are shown in SI Table S2.

The forward scattered SHG was collected via aspheric condenser lens (NA 0.79, F = 16 mm) and subject to a pair of filters to remove the input pump and the higher order harmonic generations identical to the reflection mode setup. The total average power of the forward scattered SHG is then determined by accounting for the power loss through each optical component, listed in SI Table S2. The aspheric condenser lens was replaced with a $60 \times$ objective (Nikon, M Plan 60,

630770) when taking the forward scattered images to obtain the farfield pattern.

Analytical Modeling. The average unit-cell size of the nanowires at the outer interface of the particle is subwavelength. Hence, we can approximate the nanowires using an effective medium approach. Since the nanowires are mostly oriented radially, we can model them with all-dielectric radial anisotropy using Maxwell-Garnett approximation. The effective permittivity parallel and normal to the direction of the nanowires are ⁵²

$$\varepsilon_{\perp} = \rho(r)\varepsilon_d + (1 - \rho(r))\varepsilon_h$$

$$\varepsilon_{\parallel} = \frac{(1 + \rho(r))\varepsilon_{d}\varepsilon_{h} + (1 - \rho(r))\varepsilon_{h}^{2}}{(1 - \rho(r))\varepsilon_{d} + (1 + \rho(r))\varepsilon_{h}}$$

where $\varepsilon_{\rm d}$ is the permittivity of the dielectric nanowire, $\varepsilon_{\rm h}$ is the permittivity of the host medium (which is air here), and $\rho(r)$ is the nanowire filling factor. Since the density of the nanowires reduces as the distance from the center increases, the filling factor is r-dependent. This results in a graded-index profile in the shell. For the TE (magnetic) modes, the electric field in the r direction is zero. Hence, the TE modes do not feel the anisotropy of the shell. However, the TM (electric) modes are affected by the anisotropy of the shell.

To calculate the scattered fields, we have used the Mie theory. We have assumed the input is a plane wave polarized in the x direction and propagates in the z direction. The input electric field intensity is E_0 . The electric and magnetic fields of TE and TM modes in the r direction in the mth-medium can be written as 53

$$E_r^m(r, \theta, \varphi) = \frac{E_0}{k_0^2 r^2} \cos \varphi \sum_n i^{(n+1)} (2n+1) a_n^m z_{n_{e,m}} (k_0 \sqrt{\varepsilon_{\perp,m}} r)$$

$$P^{(1)}(\cos \theta)$$

$$H_r^m(r, \theta, \varphi) = \frac{E_0}{Z_0 k_0^2 r^2} \cos \varphi \sum_n i^{(n+1)} (2n+1) b_n^m z_n (k_0 \sqrt{\varepsilon_{\perp,m}} r) P_n^{(1)}(\cos \theta)$$

where a_n^m and (b_n^m) are constants representing normalized field amplitude of nth electric and magnetic modes in the mth medium, respectively. z_n (x) is one of the Ricatti-Bessel functions of nth-order or their superposition, $P_n^{(1)}$ is associate Legendre function of 1st order and nth degree, $\varepsilon_{\perp,m} = \varepsilon_{\theta,m} = \varepsilon_{\phi,m}$ and $\varepsilon_{\parallel,m} = \varepsilon_{r,m}$ are the transverse and longitudinal components of the effective permittivity of the mth-medium, respectively, and k_0 and Z_0 are the wavenumber and the impedance of the frees-pace, respectively. The order of the Bessel functions in anisotropic media is

$$n_{\varepsilon,m} = \sqrt{\frac{\varepsilon_{\perp,m}}{\varepsilon_{\parallel,m}}n(n+1) + \frac{1}{4}} - \frac{1}{2}$$

The normalized amplitude of the scattered filed of the nth mode in free space are defined as scattering coefficients of electric (a_n) and magnetic (b_n) modes. It is seen that by changing the anisotropy, we can control the index of the Bessel function for the electric modes.

To model the graded-index profile, we have discretized the metamaterial shell to 40 homogeneous layers. By applying the boundary conditions at the interface between each layer, we can find the scattering coefficients of the particle with metamaterial shell.

ASSOCIATED CONTENT

Supporting Information

The Supporting Information is available free of charge at https://pubs.acs.org/doi/10.1021/acsnano.0c07127.

Part 1: Experiment - construction of meta-shell supraparticles (MSP); Part 2: FDTD simulations — extinction cross-section; Part 3: FDTD simulations — Photonic nanojet in MSP; Part 4: Analytical Calculations; Part 5: FDTD simulations — Nonlinear optics with MSP; Part 6: Experiment — Confocal microscopy; Part 7: Experi-

ment - Nonlinear optical microscopy; Part 8: Additional analytical calculations; Part 9: References (PDF)

AUTHOR INFORMATION

Corresponding Author

Alireza Marandi — Department of Electrical Engineering, California Institute of Technology, Pasadena, California 91107, United States; orcid.org/0000-0002-0470-0050; Email: marandi@caltech.edu

Authors

Joong Hwan Bahng — Department of Electrical Engineering, California Institute of Technology, Pasadena, California 91107, United States; © orcid.org/0000-0003-0997-9625

Saman Jahani – Department of Electrical Engineering, California Institute of Technology, Pasadena, California 91107, United States

Douglas G. Montjoy — Department of Chemical Engineering, University of Michigan, Ann Arbor, Michigan 48109, United States; © orcid.org/0000-0003-3675-8596

Timothy Yao — Department of Electrical Engineering, California Institute of Technology, Pasadena, California 91107, United States

Nicholas Kotov — Department of Chemical Engineering, University of Michigan, Ann Arbor, Michigan 48109, United States; © orcid.org/0000-0002-6864-5804

Complete contact information is available at: https://pubs.acs.org/10.1021/acsnano.0c07127

Author Contributions

The manuscript was written through contributions of all authors.

Author Contributions

§J.H.B. and S.J. contributed equally

Notes

The authors declare no competing financial interest.

ACKNOWLEDGMENTS

We thank Caltech Biological Imaging Facility - Beckman Institute for granting access to the confocal microscopes. We also thank the staff members (Dr. Andre Collazo and Dr. Giada Spigolon) for their support in the confocal microscopy. We acknowledge support from NSF Grant No. 1846273.

REFERENCES

- (1) Schauermann, S.; Nilius, N.; Shaikhutdinov, S.; Freund, H.-J. Nanoparticles for Heterogeneous Catalysis: New Mechanistic Insights. *Acc. Chem. Res.* **2013**, 46 (8), 1673–1681.
- (2) Gao, D.; Arán-Ais, R. M.; Jeon, H. S.; Roldan Cuenya, B. Rational Catalyst and Electrolyte Design for CO2 Electroreduction towards Multicarbon Products. *Nat. Catal.* **2019**, 2 (3), 198–210.
- (3) Peer, D.; Karp, J. M.; Hong, S.; Farokhzad, O. C.; Margalit, R.; Langer, R. Nanocarriers as an Emerging Platform for Cancer Therapy. *Nat. Nanotechnol.* **2007**, *2*, 751.
- (4) Smith, B. R.; Gambhir, S. S. Nanomaterials for *in Vivo* Imaging. *Chem. Rev.* **2017**, *117* (3), 901–986.
- (5) Howes, P. D.; Chandrawati, R.; Stevens, M. M. Colloidal Nanoparticles as Advanced Biological Sensors. *Science* **2014**, *346* (6205), 1247390.
- (6) Lohse, S. E.; Murphy, C. J. Applications of Colloidal Inorganic Nanoparticles: From Medicine to Energy. *J. Am. Chem. Soc.* **2012**, *134* (38), 15607–15620.
- (7) Cho, K.-S.; Lee, E. K.; Joo, W.-J.; Jang, E.; Kim, T.-H.; Lee, S. J.; Kwon, S.-J.; Han, J. Y.; Kim, B.-K.; Choi, B. L.; Kim, J. M. High-

- Performance Crosslinked Colloidal Quantum-Dot Light-Emitting Diodes. *Nat. Photonics* **2009**, *3* (6), 341–345.
- (8) Fernandez-Bravo, A.; Wang, D.; Barnard, E. S.; Teitelboim, A.; Tajon, C.; Guan, J.; Schatz, G. C.; Cohen, B. E.; Chan, E. M.; Schuck, P. J.; Odom, T. W. Ultralow-Threshold, Continuous-Wave Upconverting Lasing from Subwavelength Plasmons. *Nat. Mater.* **2019**, *18* (11), 1172–1176.
- (9) Nie, Z.; Petukhova, A.; Kumacheva, E. Properties and Emerging Applications of Self-Assembled Structures Made from Inorganic Nanoparticles. *Nat. Nanotechnol.* **2010**, *5*, 15.
- (10) Smith, A. M.; Mancini, M. C.; Nie, S. Second Window for in Vivo Imaging. Nat. Nanotechnol. 2009, 4, 710.
- (11) Weissleder, R. A Clearer Vision for in Vivo Imaging. Nat. Biotechnol. 2001, 19 (4), 316-317.
- (12) Idris, N. M.; Gnanasammandhan, M. K.; Zhang, J.; Ho, P. C.; Mahendran, R.; Zhang, Y. *In Vivo* Photodynamic Therapy Using Upconversion Nanoparticles as Remote-Controlled Nanotransducers. *Nat. Med.* **2012**, *18* (10), 1580–1585.
- (13) Wen, S.; Zhou, J.; Schuck, P. J.; Suh, Y. D.; Schmidt, T. W.; Jin, D. Future and Challenges for Hybrid Upconversion Nanosystems. *Nat. Photonics* **2019**, *13* (December). 828.
- (14) Kachynski, A. V.; Pliss, A.; Kuzmin, A. N.; Ohulchanskyy, T. Y.; Baev, A.; Qu, J.; Prasad, P. N. Photodynamic Therapy by *in Situ* Nonlinear Photon Conversion. *Nat. Photonics* **2014**, *8*, 455.
- (15) Ravetz, B. D.; Pun, A. B.; Churchill, E. M.; Congreve, D. N.; Rovis, T.; Campos, L. M. Photoredox Catalysis Using Infrared Light via Triplet Fusion Upconversion. Nature 2019, 565 (7739), 343–346. (16) Jahani, S.; Jacob, Z. All-Dielectric Metamaterials. Nat. Nanotechnol. 2016, 11 (1), 23–36.
- (17) Kuznetsov, A. I.; Miroshnichenko, A. E.; Brongersma, M. L.; Kivshar, Y. S.; Luk'yanchuk, B. Optically Resonant Dielectric Nanostructures. *Science* **2016**, 354 (6314), aag2472.
- (18) Smirnova, D.; Kivshar, Y. S. Multipolar Nonlinear Nanophotonics. *Optica* **2016**, 3 (11), 1241–1255.
- (19) Baranov, D. G.; Zuev, D. A.; Lepeshov, S. I.; Kotov, O. V.; Krasnok, A. E.; Evlyukhin, A. B.; Chichkov, B. N. All-Dielectric Nanophotonics: The Quest for Better Materials and Fabrication Techniques. *Optica* **2017**, *4* (7), 814–825.
- (20) Koshelev, K.; Kruk, S.; Melik-Gaykazyan, E.; Choi, J.-H.; Bogdanov, A.; Park, H.-G.; Kivshar, Y. Subwavelength Dielectric Resonators for Nonlinear Nanophotonics. *Science* **2020**, 367 (6475), 288LP–292.
- (21) Shcherbakov, M. R.; Neshev, D. N.; Hopkins, B.; Shorokhov, A. S.; Staude, I.; Melik-Gaykazyan, E. V.; Decker, M.; Ezhov, A. A.; Miroshnichenko, A. E.; Brener, I.; Fedyanin, A. A.; Kivshar, Y. S. Enhanced Third-Harmonic Generation in Silicon Nanoparticles Driven by Magnetic Response. *Nano Lett.* **2014**, *14* (11), 6488–6492.
- (22) Yang, Y.; Wang, W.; Boulesbaa, A.; Kravchenko, I. I.; Briggs, D. P.; Puretzky, A.; Geohegan, D.; Valentine, J. Nonlinear Fano-Resonant Dielectric Metasurfaces. *Nano Lett.* **2015**, *15* (11), 7388–7393.
- (23) Carletti, L.; Locatelli, A.; Stepanenko, O.; Leo, G.; Angelis, C. D. Enhanced Second-Harmonic Generation from Magnetic Resonance in AlGaAs Nanoantennas. *Opt. Express* **2015**, *23* (20), 26544–26550
- (24) Gili, V. F.; Carletti, L.; Locatelli, A.; Rocco, D.; Finazzi, M.; Ghirardini, L.; Favero, I.; Gomez, C.; Lemaître, A.; Celebrano, M.; Angelis, C. D.; Leo, G. Monolithic AlGaAs Second-Harmonic Nanoantennas. *Opt. Express* **2016**, 24 (14), 15965–15971.
- (25) Grinblat, G.; Li, Y.; Nielsen, M. P.; Oulton, R. F.; Maier, S. A. Enhanced Third Harmonic Generation in Single Germanium Nanodisks Excited at the Anapole Mode. *Nano Lett.* **2016**, *16* (7), 4635–4640.
- (26) Shcherbakov, M. R.; Shorokhov, A. S.; Neshev, D. N.; Hopkins, B.; Staude, I.; Melik-Gaykazyan, E. V.; Ezhov, A. A.; Miroshnichenko, A. E.; Brener, I.; Fedyanin, A. A.; Kivshar, Y. S. Nonlinear Interference and Tailorable Third-Harmonic Generation from Dielectric Oligomers. ACS Photonics 2015, 2 (5), 578–582.

- (27) Krasnok, A.; Tymchenko, M.; Alù, A. Nonlinear Metasurfaces: A Paradigm Shift in Nonlinear Optics. *Mater. Today* **2018**, *21* (1), 8–21.
- (28) Pertsch, T.; Kivshar, Y. Nonlinear Optics with Resonant Metasurfaces. MRS Bull. 2020, 45 (3), 210–220.
- (29) Marino, G.; Solntsev, A. S.; Xu, L.; Gili, V. F.; Carletti, L.; Poddubny, A. N.; Rahmani, M.; Smirnova, D. A.; Chen, H.; Lemaître, A.; Zhang, G.; Zayats, A. V.; De Angelis, C.; Leo, G.; Sukhorukov, A. A.; Neshev, D. N. Spontaneous Photon-Pair Generation from a Dielectric Nanoantenna. *Optica* **2019**, *6* (11), 1416–1422.
- (30) Kruk, S.; Poddubny, A.; Smirnova, D.; Wang, L.; Slobozhanyuk, A.; Shorokhov, A.; Kravchenko, I.; Luther-Davies, B.; Kivshar, Y. Nonlinear Light Generation in Topological Nanostructures. *Nat. Nanotechnol.* **2019**, *14* (2), 126–130.
- (31) Yang, Y.; Wang, W.; Boulesbaa, A.; Kravchenko, I. I.; Briggs, D. P.; Puretzky, A.; Geohegan, D.; Valentine, J. Nonlinear Fano-Resonant Dielectric Metasurfaces. *Nano Lett.* **2015**, *15* (11), 7388–7393.
- (32) Xu, L.; Saerens, G.; Timofeeva, M.; Smirnova, D. A.; Volkovskaya, I.; Lysevych, M.; Camacho-Morales, R.; Cai, M.; Zangeneh Kamali, K.; Huang, L.; Karouta, F.; Tan, H. H.; Jagadish, C.; Miroshnichenko, A. E.; Grange, R.; Neshev, D. N.; Rahmani, M. Forward and Backward Switching of Nonlinear Unidirectional Emission from GaAs Nanoantennas. *ACS Nano* **2020**, *14* (2), 1379–1389.
- (33) Saerens, G.; Tang, I.; Petrov, M. I.; Frizyuk, K.; Renaut, C.; Timpu, F.; Escalé, M. R.; Shtrom, I.; Bouravleuv, A.; Cirlin, G.; Grange, R.; Timofeeva, M. Engineering of the Second-Harmonic Emission Directionality with III–V Semiconductor Rod Nanoantennas. *Laser Photonics Rev.* 2020, 14 (9), 2000028.
- (34) Gigli, C.; Wu, T.; Marino, G.; Borne, A.; Leo, G.; Lalanne, P. Quasinormal-Mode Non-Hermitian Modeling and Design in Nonlinear Nano-Optics. *ACS Photonics* **2020**, *7* (5), 1197–1205.
- (35) Kim, E.; Steinbrück, A.; Buscaglia, M. T.; Buscaglia, V.; Pertsch, T.; Grange, R. Second-Harmonic Generation of Single BaTiO3 Nanoparticles down to 22 Nm Diameter. *ACS Nano* **2013**, *7* (6), 5343–5349.
- (36) Dutto, F.; Raillon, C.; Schenk, K.; Radenovic, A. Nonlinear Optical Response in Single Alkaline Niobate Nanowires. *Nano Lett.* **2011**, *11* (6), 2517–2521.
- (37) Pu, Y.; Grange, R.; Hsieh, C.-L.; Psaltis, D. Nonlinear Optical Properties of Core-Shell Nanocavities for Enhanced Second-Harmonic Generation. *Phys. Rev. Lett.* **2010**, *104* (20), 207402.
- (38) Ali, R. F.; Bilton, M.; Gates, B. D. One-Pot Synthesis of Sub-10 Nm LiNbO3 Nanocrystals Exhibiting a Tunable Optical Second Harmonic Response. *Nanoscale Adv.* **2019**, *1* (6), 2268–2275.
- (39) Sergeyev, A.; Geiss, R.; Solntsev, A. S.; Sukhorukov, A. A.; Schrempel, F.; Pertsch, T.; Grange, R. Enhancing Guided Second-Harmonic Light in Lithium Niobate Nanowires. *ACS Photonics* **2015**, 2 (6), 687–691.
- (40) Bahng, J. H.; Yeom, B.; Wang, Y.; Tung, S. O.; Hoff, J. D.; Kotov, N. Anomalous Dispersions of "hedgehog" Particles. *Nature* **2015**, *517* (7536), 596–599.
- (41) Montjoy, D. G.; Bahng, J. H.; Eskafi, A.; Hou, H.; Kotov, N. A. Omnidispersible Hedgehog Particles with Multilayer Coatings for Multiplexed Biosensing. *J. Am. Chem. Soc.* **2018**, *140* (25), 7835–7845.
- (42) Kirchner, S. R.; Su, M. N.; Bahng, J. H.; Montjoy, D. G.; Chang, W. S.; Kotov, N.; Link, S. Scattering Properties of Individual Hedgehog Particles. *J. Phys. Chem. C* **2018**, *122* (22), 12015–12021.
- (43) Larciprete, M. C.; Centini, M. Second Harmonic Generation from ZnO Films and Nanostructures. *Appl. Phys. Rev.* **2015**, 2 (3), 31302.
- (44) Sheverdin, A.; Valagiannopoulos, C. Core-Shell Nanospheres under Visible Light: Optimal Absorption, Scattering, and Cloaking. *Phys. Rev. B: Condens. Matter Mater. Phys.* **2019**, 99 (7), 075305.
- (45) Luk'yanchuk, B. S.; Paniagua-Domínguez, R.; Minin, I.; Minin, O.; Wang, Z. Refractive Index Less than Two: Photonic Nanojets

- Yesterday, Today and Tomorrow [Invited]. Opt. Mater. Express 2017, 7 (6), 1820.
- (46) Chen, Z.; Taflove, A.; Backman, V. Photonic Nanojet Enhancement of Backscattering of Light by Nanoparticles: A Potential Novel Visible-Light Ultramicroscopy Technique. *Opt. Express* **2004**, *12* (7), 1214–1220.
- (47) Lecler, S.; Takakura, Y.; Meyrueis, P. Properties of a Three-Dimensional Photonic Jet. Opt. Lett. 2005, 30 (19), 2641–2643.
- (48) Wang, Z.; Guo, W.; Li, L.; Luk'yanchuk, B.; Khan, A.; Liu, Z.; Chen, Z.; Hong, M. Optical Virtual Imaging at 50 Nm Lateral Resolution with a White-Light Nanoscope. *Nat. Commun.* **2011**, 2 (1), 218.
- (49) Yue, L.; Minin, O. V.; Wang, Z.; Monks, J. N.; Shalin, A. S.; Minin, I. V. Photonic Hook: A New Curved Light Beam. *Opt. Lett.* **2018**, 43 (4), 771–774.
- (50) Minin, I. V.; Minin, O. V.; Katyba, G. M.; Chernomyrdin, N. V.; Kurlov, V. N.; Zaytsev, K. I.; Yue, L.; Wang, Z.; Christodoulides, D. N. Experimental Observation of a Photonic Hook. *Appl. Phys. Lett.* **2019**, *114* (3), 031105.
- (51) Grandidier, J.; Callahan, D. M.; Munday, J. N.; Atwater, H. A. Light Absorption Enhancement in Thin-Film Solar Cells Using Whispering Gallery Modes in Dielectric Nanospheres. *Adv. Mater.* **2011**, 23 (10), 1272–1276.
- (52) Jahani, S.; Jacob, Z. Transparent Subdiffraction Optics: Nanoscale Light Confinement without Metal. *Optica* **2014**, *1* (2), 96–100.
- (53) Qiu, C.-W.; Luk'yanchuk, B. Peculiarities in Light Scattering by Spherical Particles with Radial Anisotropy. *J. Opt. Soc. Am. A* **2008**, 25 (7), 1623–1628.
- (54) Liu, W. Ultra-Directional Super-Scattering of Homogenous Spherical Particles with Radial Anisotropy. *Opt. Express* **2015**, 23 (11), 14734–14743.
- (55) Palmer, B. A.; Yallapragada, V. J.; Schiffmann, N.; Wormser, E. M.; Elad, N.; Aflalo, E. D.; Sagi, A.; Weiner, S.; Addadi, L.; Oron, D. A Highly Reflective Biogenic Photonic Material from Core—Shell Birefringent Nanoparticles. *Nat. Nanotechnol.* **2020**, *15* (2), 138–144.
- (56) Jahani, S.; Kim, S.; Atkinson, J.; Wirth, J. C.; Kalhor, F.; Noman, A. Al; Newman, W. D.; Shekhar, P.; Han, K.; Van, V.; DeCorby, R. G.; Chrostowski, L.; Qi, M.; Jacob, Z. Controlling Evanescent Waves Using Silicon Photonic All-Dielectric Metamaterials for Dense Integration. *Nat. Commun.* **2018**, *9* (1), 1893.
- (57) Rho, J.; Ye, Z.; Xiong, Y.; Yin, X.; Liu, Z.; Choi, H.; Bartal, G.; Zhang, X. Spherical Hyperlens for Two-Dimensional Sub-Diffractional Imaging at Visible Frequencies. *Nat. Commun.* **2010**, *1* (1), 143.
- (58) Kabashin, A. V.; Evans, P.; Pastkovsky, S.; Hendren, W.; Wurtz, G. A.; Atkinson, R.; Pollard, R.; Podolskiy, V. A.; Zayats, A. V. Plasmonic Nanorod Metamaterials for Biosensing. *Nat. Mater.* **2009**, 8 (11), 867–871.
- (59) Shekhar, P.; Atkinson, J.; Jacob, Z. Hyperbolic Metamaterials: Fundamentals and Applications. *Nano Converg* **2014**, *1* (1), 14.
- (60) Shekhar, P.; Pendharker, S.; Sahasrabudhe, H.; Vick, D.; Malac, M.; Rahman, R.; Jacob, Z. Extreme Ultraviolet Plasmonics and Cherenkov Radiation in Silicon. *Optica* **2018**, *5* (12), 1590–1596.
- (61) Jahani, S.; Roy, A.; Marandi, A. Wavelength-Scale Optical Parametric Oscillators. *ArXiv200413943 Phys.* **2020**.
- (62) Dhara, S., Lynch, S. A. Chapter 2, Second Harmonic Generation in ZnO Nanowires. Nanowires New Insights. *IntechOpen.* **2017**. Open access peer-reviewed Edited Volume.
- (63) Evlyukhin, A. B.; Nerkararyan, K. V.; Bozhevolnyi, S. I. Core-Shell Particles as Efficient Broadband Absorbers in Infrared Optical Range. Opt. Express 2019, 27 (13), 17474–17481.
- (64) Zhang, Y.; Grady, N. K.; Ayala-Orozco, C.; Halas, N. J. Three-Dimensional Nanostructures as Highly Efficient Generators of Second Harmonic Light. *Nano Lett.* **2011**, *11* (12), 5519–5523.
- (65) Yang, Z.; Wang, M.; Shukla, S.; Zhu, Y.; Deng, J.; Ge, H.; Wang, X.; Xiong, Q. Developing Seedless Growth of ZnO Micro/Nanowire Arrays towards ZnO/FeS 2 /CuI P-I-N Photodiode Application. Sci. Rep. 2015, 5 (1), 11377.

- (66) Douglas, M., Bahng, J. H., Eskafi, A., Hou, H., Jiang, R., Kotov, N. A. Photocatalytic Hedgehog Particles for High Ionic Strength Environment, in press.
- (67) Das, S. K.; Bock, M.; O'Neill, C.; Grunwald, R.; Lee, K. M.; Lee, H. W.; Lee, S.; Rotermund, F. Efficient Second Harmonic Generation in ZnO Nanorod Arrays with Broadband Ultrashort Pulses. *Appl. Phys. Lett.* **2008**, 93 (18), 181112.